Surface modification of W-V alloy exposed to high heat flux helium neutral beams

Jun Wang[1], Chun Li[2], Yue Yuan[1,*], Henri Greuner[3], Long Cheng[1], Guang-Hong Lu[1]

[1] School of Physics and Nuclear Energy Engineering, Beihang University, Beijing 100091, China

[2] College of Mechanical and Materials Engineering, North China University of Technology, Beijing 100144, China

[3] Max Planck Institute for Plasma Physics, Boltzmannstr. 2, 85748 Garching, Germany

[*] Correspondence: yueyuan@buaa.edu.cn

Abstract: Surface modification of tungsten vanadium (W-V) alloy under high heat flux helium particle bombardment has been studied. W-5 wt.% V samples were irradiated by the repeated helium pulses at a peak surface temperature of 900 °C and 1800 °C, respectively, in the neutral beam facility GLADIS. The effect of helium fluence on the surface morphology changes was investigated by increasing helium fluence from 1×10^{22} m^{-2} to 2×10^{22} m^{-2}. Blister is the typical structure after the repeated helium pulses loading at 900 °C, and it gets more severe with the increased fluence. Porous structure turns to be dominant at 1800 °C. An evolution of porous structure to coral-like structure is observed as fluence increases. In addition, the three typical regions in W-5V, W-enriched region, W-V solid solute region and V-enriched region, exhibit different damage features. W-V solid solute region shows better surface damage resistance compared to the other two regions.

Key words: W-V alloy, helium, high heat flux, surface modification

1. Introduction

Tungsten (W) is chosen as a plasma facing material (PFM) in fusion devices due to its high melting point, high thermal stability and low sputtering yield [1]. However, its low temperature brittleness and high ductile-brittle transition temperature (DBTT) significantly affect the performance of W-PFM [2]. W-PFM will be subjected to extreme conditions in fusion devices, like high heat flux loading and high flux particle bombardment (hydrogen (H) isotopes and helium (He)) [3]. High heat flux loading can result in surface roughening, cracking and melting, which significantly degrade both mechanical and thermal properties and can reduce the lifetime of PFMs. He particle loading causes the formation of nanometric bubble layers in the subsurface, and results in significantly surface morphology changes and property degradation of W [4]. As a result, the cracking resistance is significantly reduced due to the increase in brittleness and the decrease in effective thermal conductivity [5,6]. Simultaneous high heat flux and particle loading can lead to more severe damage [7].

In order to develop an advanced W-based material which has sufficient mechanical properties to keep structure sound in the fusion environment, different ductilization and toughening ways have been investigated [3]. Alloying with ductile components and refining W microstructure are two of the most promising ways. Vanadium (V) is a ductile metal which has unrestricted dissolution in W, and it is added for W-based material enhancement. According to the previous studies [8,9], W-V alloy shows a refined microstructure and better mechanical properties than W, but how W-V alloy behaves under simultaneous heat and He loading is less

known. In this work, W-V alloy is exposed to high heat flux He neutral beams. The damage resistance of the different regions in W-V alloy is compared with one another, and the evolution of surface morphology with increasing peak surface temperature and particle fluence is investigated.

2. Experiments

W- 5 wt.% V was fabricated by powder metallurgy. W powders (2 μm) and V powders (0.8 μm) with purity > 99.9% were mixed in a blender for 8 h. The mixed powder was initially compacted by cold isotopic pressing, then the mixed powder was sintered in a hydrogen furnace. The furnace was heated to a peak temperature of 1800 °C and kept at this temperature for 2 h, and the bulk was cooled down in the furnace under hydrogen atmosphere [10]. All tested samples were cut to a size of 10 × 10 × 3 mm^3 from the bulk. Surfaces were ground by SiC sandpaper and then mechanically polished to mirror-like finish. The alloying characteristics were observed by scanning electron microscopy (SEM) and energy dispersive spectroscopy (EDS).

He neutral beam exposures were carried in the neutral beam high heat flux test facility GLADIS (Garching Large Divertor Sample Test Facility) at IPP-Garching [11]. The neutral beam facility GLADIS has the capability to apply H, He or mixed H/He beam with a heat flux < 45 MW m^{-2} up to 45 s pulse length. The full width of the Gaussian beam at 80% central power density is 70 mm. Surface temperature was recorded by pyrometers and an IR camera. More details can be found in [11–15]. In this study we performed an adiabatic He loading on the samples with He particle energy of 22 keV, a central heat flux of 3 MW/m^2 and a particle flux of 7 × 10^{20} He $m^{-2}s^{-1}$. We increased the peak surface temperature from 900 to 1800 °C by extending the pulse duration, and increased He fluence from 1 × 10^{22} to 2 × 10^{22} m^{-2} by increasing pulses. The main experimental parameters are listed in Table 1.

Table.1 The main parameters of the repeated He pulses at GLADIS

Peak surface temperature [°C]	Ion energy [k eV]	Flux [He $m^{-2}s^{-1}$]	Pulse duration [s]	Number of pulses	Fluence [He m^{-2}]
900	22	7 × 10^{20}	1.5	10	1 × 10^{22}
900	22	7 × 10^{20}	1.5	20	2 ×10^{22}
1800	22	7 × 10^{20}	4.7	3	1 × 10^{22}
1800	22	7 × 10^{20}	4.7	6	2 ×10^{22}

After exposure, the surface morphology was investigated by SEM combined with focused ion beam (FIB) milling. Backscattered electron (BSE) imaging was performed to distinguish different phases regions in W-V alloy.

Simulation of He projected range was performed by SRIM [16]. The calculated depth distributions of He in W and V after exposures with a fluence of 1 × 10^{22} m^{-2} are shown in Figure 1. The maximum projected range of He in W is about 150 nm, and with a peak at 50 nm. While projected range of He in V is much deeper than that in W, where the maximum projected range is about 230 nm and with a peak at 110 nm.

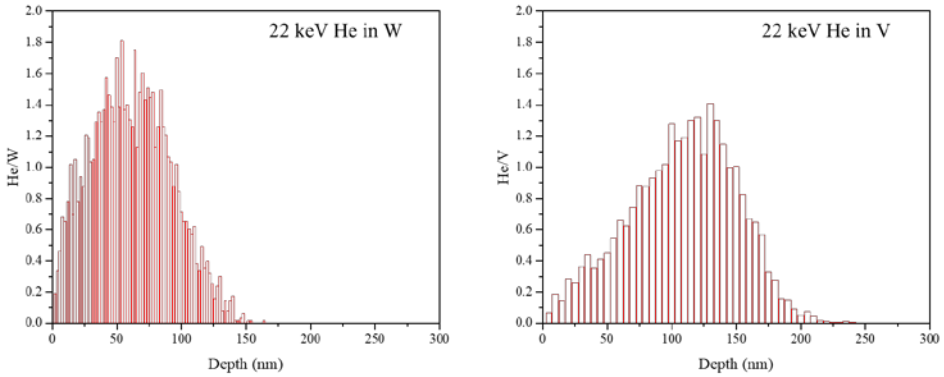

Figure 1. SRIM simulation of Helium depth distributions after energetic He bombardment in W and V with an incident energy of 22 keV and fluence of 1×10^{22} m^{-2}.

3. Results

3.1 W-5V surface before exposure

SEM and EDS images of W-5V polished surface before exposure are shown in Figure 2. According to the results of EDS, three typical regions can be clearly distinguished in the W-5V, which are the W-enriched region, the W-V solid solute region and the V-enriched region. We use ○,1○,2○,3 to mark the W-enriched region, the W-V solid solute region and the V-enriched region respectively in the Figure 2, as well as the other figures shown in this paper. The formation of the V-enriched region can be attributed to the limited V diffusion at the low sintering temperature of 1800 °C. Due to the low content of V (5 wt.%) in the alloy, the V-enriched region only contributes to a small area fraction of the polished surface. Pores from the fabrication can be observed on the polished surface of the sintered sample, and the size of pores ranged from hundreds nanometers to several micrometers and the average size was about 1 μm. We believe the pre-existing fabrication pores play a minor role on the He-induced surface modification. In addition, the average grain size of W-5V was about 24 μm [10], which was much larger than He projected range.

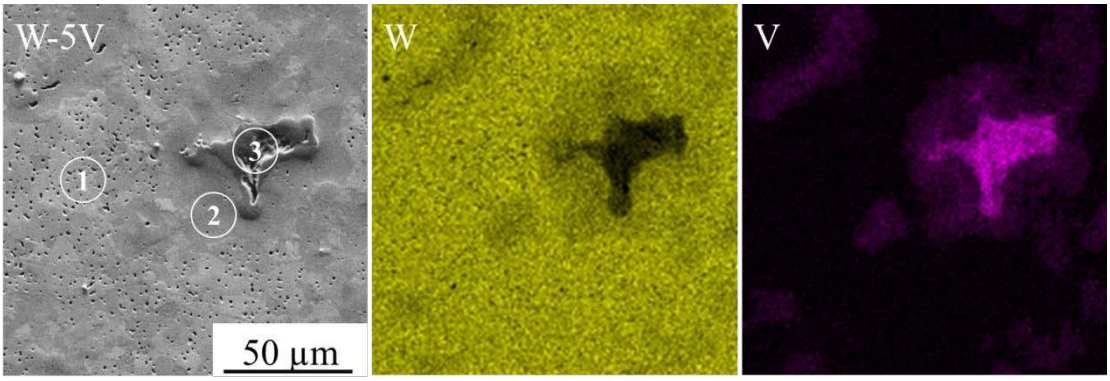

Figure 2. SEM and EDS images of W-5V surface before exposure. ○,1 W-enriched region, ○,2 W-V solid solute region and ○,3 V-enriched region.

3.2 Surface modification after He loading at a peak surface temperature of 900 °C

After He loading at a peak surface temperature of 900 °C with a fluence of 1×10^{22} m^{-2}, a large number of blisters are observed on the exposed surface, as shown in Figure 3. Blistering on W is widely reported in previous study [17–19]. Blistering on the W-5V shows some differences due to the three typical phase regions. In the W-enriched region, blisters with various sizes and different structures are observed. The blister size is varied from a few hundreds of nanometres to several micrometres. Although some of the blisters still keep their structure intact, most of blisters are ruptured and the lids of some ruptured blisters are totally exfoliated from the surface. Craters with a rough planar base are left after the blister lid exfoliation. Large craters with diameter up to 6 µm are observed on the W-enriched region as shown in Figure 3a. Moreover, slip bands can be observed during the lid exfoliation (Figure 3c), which is attributed to the plastic deformation. It should be noted that blisters without rupture usually show roughly circular shape (Figure 3e), but craters feature various shapes (Figure 3c and 3d).

Blisters on the surface of W-V solid solute region show a much smaller area density compared to that in W-enriched region (Figure 3a). The fraction of ruptured blisters in W-V solid solute region is lower than W-enriched region. Large craters with size up to 4 µm also can be found on W-V solid solute region, but both the number density and the size are smaller than that on W-enriched region.

Blisters damage is more severe on the surface of V-enriched region. Large craters with sizes up to 8 µm are shown on V-enriched region (Figure 3a), and most of the craters feature a multi-layer structure (Figure 3d). Moreover, the area ratio of craters on V-enriched region is highest among these three regions.

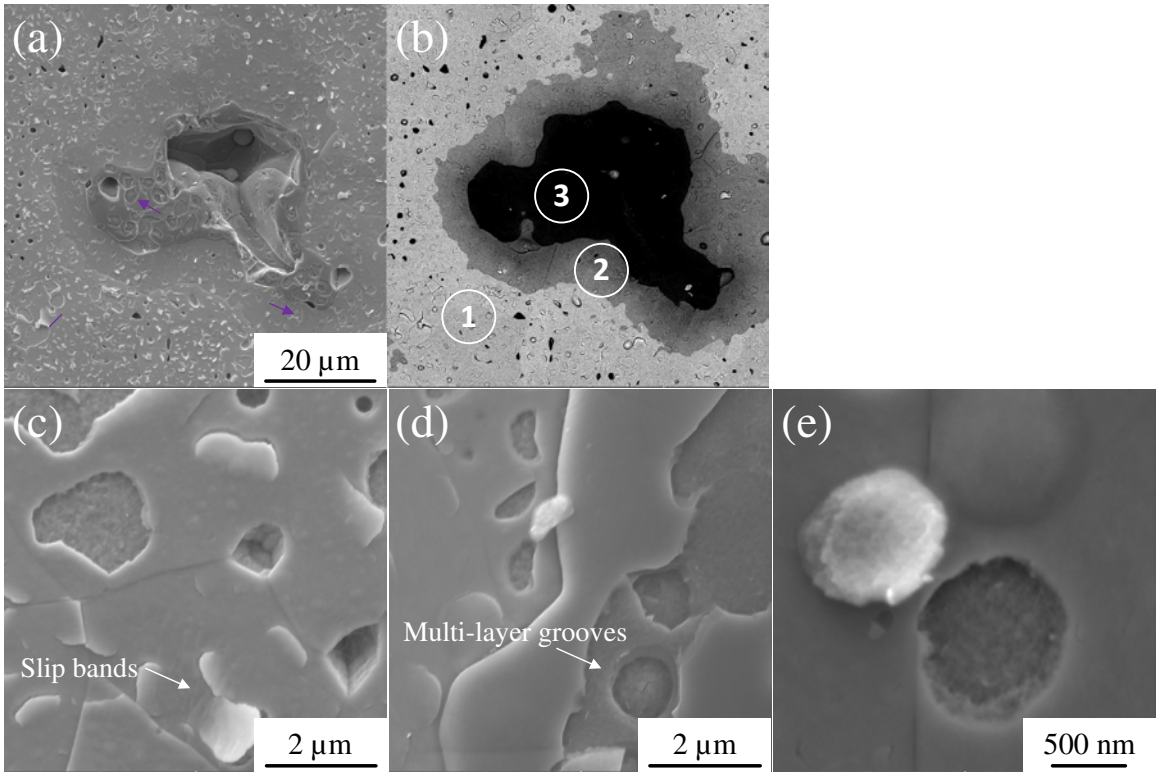

Figure 3. Surface morphology of W-5V after repeated He pulses irradiation at a peak surface temperature of 900 °C and with He fluence of 1×10^{22} m^{-2}. (a) (b) are the SE image and BSE image respectively. (c) (d) show blistering on the W-enriched region and V-enriched region, respectively. (e) is the typical circular crater formation. Purple arrows in (a) indicate large craters.

When the fluence is increased to 2×10^{22} m^{-2}, blistering on the exposed surface of W-5V becomes more severe than that under 1×10^{22} m^{-2} (Figure 4). On the W-enriched region, blister rupture and lid exfoliation are more pronounced, and craters become larger than that in the case of 1×10^{22} m^{-2}. On the V-enriched region, the multi-layer craters are 3 or 4 layers.

For the W-V solid solute region, although the area density and size of blisters increase, blistering on W-V solid solute region is still mitigated compared to the other two regions. That is to say the blistering resistance of W-V solid solute region is much better than the other two regions.

The FIB cross-sections in Figure 4 clearly show the thickness of blister lids or the depth of craters. The average thickness of lids or the depth of craters in each phase region is calculated. In the W-enriched region, the average thickness of lids is about 80 nm, and only 65 nm for the average thickness of lids on the W-V solid solute region. The average thickness of lids on V-enriched region is 130 nm, which is thickest among these three regions.

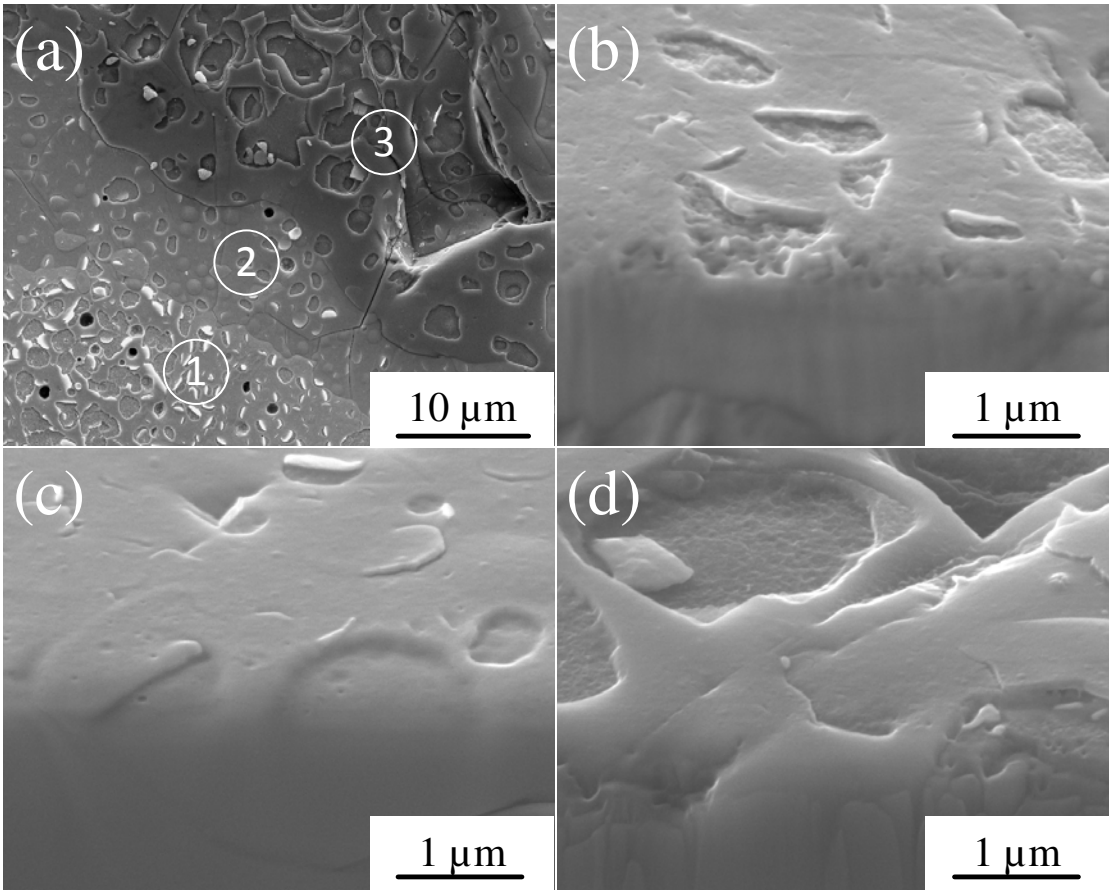

Figure 4. Surface morphology (a) and FIB cross-sections (55° tilted, b, c and d) of W-5V after repeated He pulses irradiation at a peak surface temperature of 900 °C and He fluence of 2×10^{22} m^{-2}. (b), (c) and (d) are W-enriched region, W-V solid solute region and V-enriched region respectively.

3.3 Surface modification after He loading at a high peak surface temperature of 1800 °C

Surface morphology of W-5V after the repeated He pulse loading at a peak temperature of 1800 °C and a total fluence of 1×10^{22} He m^{-2} is shown in Figure 5. A high density of pinholes is observed on the exposed surface. Surface morphology varies among the three typical regions. Porous structure is the typical microstructure on W-enriched region. While there are some differences among the different grains of W-

enriched region. Some of grains still have blisters without rupture, but a large number of pinholes can be found on the lids of blisters. Some of grains are filled with the craters with porous structure, and some of grains show coral-like structure.

A large area of lids exfoliated from the bulk can be observed on the W-V solid solute region, and large craters with high density pinholes are left on the surface. There are some grains in W-V solid solute region only show high density pinholes rather than surface layer exfoliation. These can be observed in Figure 5d, where W-V solid solute regions are in the left and show pinholes distribution combined with exfoliation (up) and no exfoliation (bottom). The surface of V-enriched region is occupied by the multi-layer craters with porous structure.

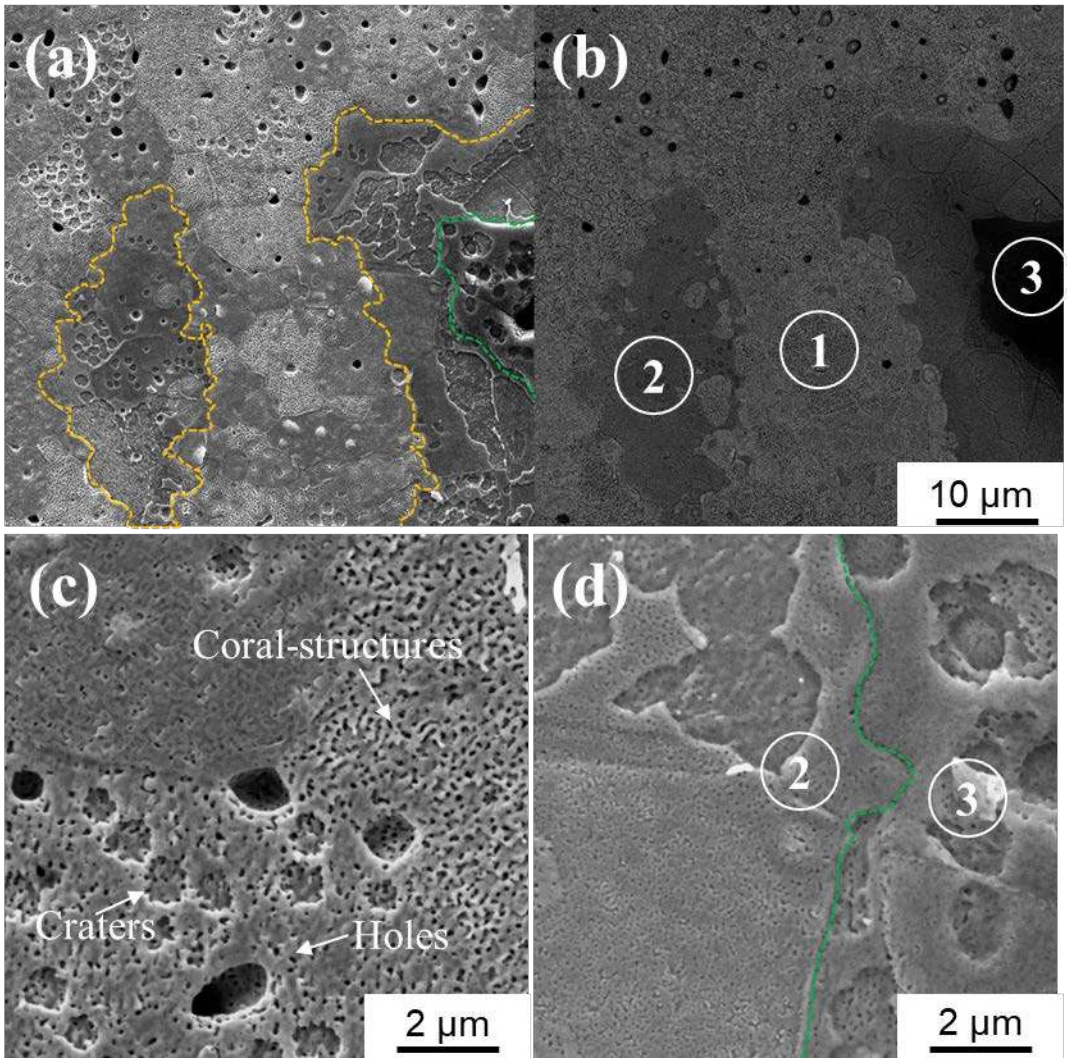

Figure 5. Surface morphology of W-5V after repeated He pulses irradiation at a peak surface temperature of 1800 °C with a He fluence of 1×10^{22} m^{-2}. (a) (b) are the SE image and BSE image represently. (c) shows the microstructure on the W-enriched region. (d) shows the microstructure on W-V solid solute region (left) and V-enriched region (right). The orange dash lines represent the boundary between W-enriched region and W-V solid solute region, and the green dash lines represent the boundary between W-V solid solute region and V-enriched region.

After repeated He pulses loading at a peak temperature of 1800 °C with a higher fluence of 2×10^{22} m^{-2}, coral-like structure becomes dominant on the exposed surface, as shown in Figure 6. An evolution of porous

structure to coral-like structure is observed. Coral-like structure (a mixture of fuzzy structure and deep holes [20]) on polycrystalline W after with similar high heat flux He neutral beams injection is widely reported, even at a higher surface temperature up to 2700 °C [11,18,19]. Coral-like structures on W-enriched region are uniformly distributed. No craters or blisters exist on the W-enriched region compared to that in 1×10^{22} m^{-2} case. For W-V solid solute region, some grains still show craters with porous structure, and other grains show coral-like structure. The microstructure evolution on the W-V solid solute is delayed compared to that on W-enriched region. For V-enriched region, besides the coral-like structure, multi-layer craters with porous structures still exist, and a part of surface starts to melt due to its low melting temperature as shown in Figure 6b.

FIB cross-sections of each region on W-5V are shown in Figure 7. The thickness of coral-like structure in W-enriched region is about 520 nm. He nanobubbles can be seen inside the coral-like structure. The thickness of coral-like structure of the W-V solid solute region is 340 nm, much thinner than that of the W-enriched region. The V-enriched region shows the thickest of coral-like structures among these three regions, which is 610 nm. The damage depth of each phase regions after He loading at 1800 °C is significantly increased compared to that at 900 °C. In general, damage depth in W-V solid solute region is much less than that of two other phase regions.

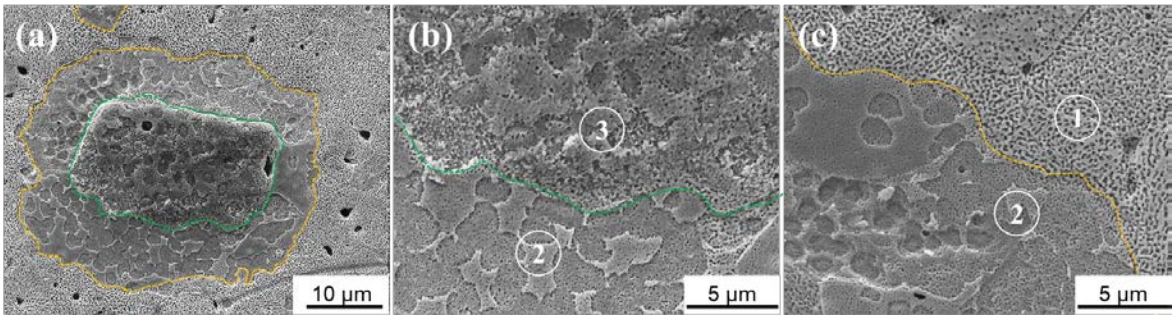

Figure 6. Surface morphology of W-5V after repeated He pulses loading at a peak surface temperature of 1800 °C with a fluence of 2×10^{22} m^{-2}. The orange dash lines represent the boundary between W-enriched region and W-V solid solute region, and the green dash lines represent the boundary between W-V solid solute region and V-enriched region.

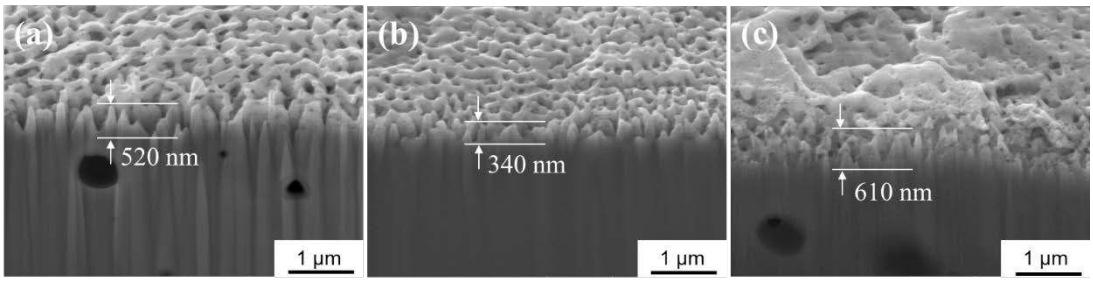

Figure 7. FIB cross-sections (55° tilted) of W-5V after repeated He pulses irradiation at a peak surface temperature of 1800 °C and He fluence of 2×10^{22} m^{-2}. (a) (b) and (c) are the W-enriched region, W-V solid solute region and V-enriched region respectively.

4. Discussion

Different surface modifications after energetic He particles with different temperature and fluence are investigated in this study. Blistering and lids exfoliation are shown on the surface of W-5V after exposed to repeated He pulses at a low peak surface temperature of 900 °C, while porous structure and coral-structure are dominant at a high peak surface temperature of 1800 °C. He bubble growth and rupture are the main factors of He-induced surface modification [20,21]. The effect of surface temperature and He fluence on He bubble evolution and surface modification is discussed.

The common feature of surface modification after repeated He pulses at a peak surface temperature of 900 °C is blistering. Blistering on the body-centred cubic metal surface such as W, V, Mo and Nb after He irradiation has been widely reported [12,19,22–24]. Mechanisms of the nucleation and growth of He bubbles have been intensively studied [18,24,25]. The nucleation of He bubbles is ascribed to self-trapping or trapping in defects like vacancies and dislocations [26]. As an electrophobic impurity, He has a positive dissolution energy in metals such as W and V and a low binding energy with other He atoms [27]. The implanted He atoms can quickly migrate in the projected range and bind with other He atoms to form small He clusters [4]. It is reported that small He clusters ($\leq$3 atoms) are very mobile at low temperatures and migrate as fast as a single He atom [28]. Once they become larger immobile He clusters, they will kick out a W self-interstitial atom then trapped by a vacancy [29]. It is very difficult for these clusters to diffuse at below 2100 K. They would tend to take part in the nucleation of He bubbles. In addition, He atoms have a high binding energy with defects (e.g. 4.5 eV with vacancy) [30]. In our study, energetic particles (22 keV He) injection can produce a high density of defects such as vacancy in the near surface layers, as shown in Figure 8. It can be seen that vacancies induced by He injection in W are distributed within the depth of 120 nm, with a peak at 35 nm. He atoms can be easily trapped by vacancies and vacancy clusters to form He_n-$(vacancies)_m$ clusters. However, He_n-$(vacancies)_m$ clusters can hardly diffuse at 900 °C and easily attract He atoms to form He bubbles. The results of TEM also show the He bubbles formation in the sub-surface around the damage depth [31]. The simulations of the nanobubble evolution in W show the nucleation and the growth of He bubbles accompanied by the formation of vacancies and dislocations, which can serve as new He trapping sites or new nuclei of He bubbles and furthermore significantly impede the He atoms penetration inward [4,25]. That is why He bubbles are usually formed at the near-surface regions. The thickness of blister lids in W-enriched region is about 80 nm, which suggests that a lot of He bubbles are formed within the damage depth.

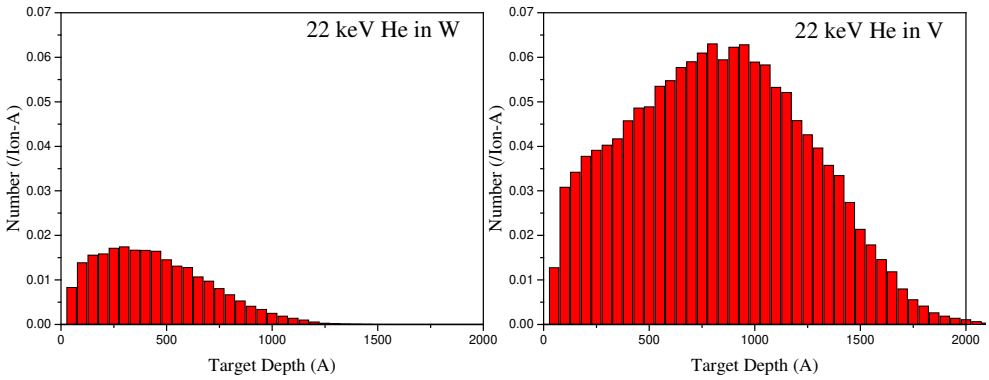

Figure 8. SRIM calculation results of the vacancy distribution in W (a) and V (b) after energetic He (22 keV) bombardment.

Moreover, He blistering on the exposed surface shows a circular shape (Figure 3). It is attributed to He bubbles coalescence [18,32,33]. The He bubbles coalescence leads to the formation of penny-shaped cavity [33]. More He atoms can be trapped by the cavity, which results in an unstable high pressure inside, it leads to the plastic deformation of the surface layer and contributes to the blister formation. The penny-shaped cavity inside enlarges and results in the circular shaped blisters. The strong stress field will be induced around the blisters and significantly reduces the strength of lids. Once the lid cannot hold the high gas pressure inside, the blisters rupture and the lids of blisters would exfoliate further. Some of blisters lids burst open then contribute to the formation of circular shaped craters (Figure 3e). While some of blisters are partially opened from one side (Figure 3c), which usually induces plastic deformation on the surface layer, and contributes to the spreading of exfoliation and leads to the formation of large craters on the exposed surface.

Craters and pinholes are the typical surface structures after low He fluence loading at intermediate temperature. The final surface morphology results from competition between blistering and porous structure formation [18]. In this study, craters and high density of pinholes are both observed after repeated He pulses irradiation at a high peak temperature of 1800 °C with a low fluence 1×10^{22} He m^{-2}, while porous structure is dominant. It is reported that bubble growth significantly proceeds when the surface temperature exceeds 1800 °C [34]. As the temperature increases to 1800 °C, large immobile He clusters would separate into small clusters. He atoms can release out from the He clusters or He-vacancy clusters in sub-surface. It significantly enhances the He diffusion. The enlarged depth distribution of He results in a deeper He bubble nuclei. Hence, a wider depth distribution of He bubbles is formed compared to that after He bombardment at 900 °C. Once bubbles in different layers contact with each other, they would coalesce and form a pinhole in the vertical direction, and then leads to porous structures formation. Therefore, the damage depth after He loading at a surface temperature of 1800 °C is deeper than that at 900 °C, which is suggested by the FIB cross-section results.

With the increase of He fluence, an evolution of porous structure to coral-like structure is observed. The increased He fluence contributes to a higher He concentration. Consequently, a higher number density of He bubbles would be formed. A higher number density of He bubbles results in a higher frequency of He bubble coalescence, which contributes to the evolution of coral-like structures. According to the discussion above, the number density and depth distribution of He bubbles are related to the He diffusion and play important roles on surface microstructure evolution.

The three typical phase regions on W-5V exhibit different surface damage resistance. W-enriched region behaves better than V-enriched region. As shown in Figure 1, the mean projected range of 22 keV He atoms in V is ~110 nm, which is much deeper than that in W (~50 nm). Moreover, the depth range of defects induced by He atoms injection in V is larger than that in W, as shown in Figure 8, which can lead to higher depth distribution of He bubbles in V-enriched region. Additionally, the density of defects after He atoms injection in V is much higher than that in W (Figure 8), which can contribute to a higher density He bubbles. The deeper depth distribution and higher number density of He bubbles contribute to severe damage in V-enriched region.

Another key phenomenon observed in this work is that surface damage on W-V solid solute region is less pronounced compared to the other two regions. Dissolved V atoms in W-V solid solute region can serve as a strong trap site of He atoms [30]. Therefore He diffusion would be greatly impeded. It would delay the nucleation of He bubbles. Additionally, solute V atoms can act as the defects sink during the energetic He

bombardment. The new generated defects would be absorbed by the solute V atoms which significantly reduces the number density of defects [30]. Consequently, less He bubbles are formed. These factors contribute to the mitigated surface damage on the W-V solid solute.

5. Conclusion

Surface morphology of W-5V after the repeated He pulse irradiation has been investigated. The results show that surface modification is strongly associated with the peak surface temperature. At 900 °C, blisters are the typical surface structure. With increased He fluence, the surface blistering is more pronounced. At 1800 °C, porous structures turn to be dominant due to the enhanced He diffusion. With the fluence increases, porous structure develops to coral-like structure. Surface damage on the exposed surface turns to be more severe as the peak surface temperature and He fluence increase.

Surface morphology in the different phase regions of W-5V is quite different to each other after the repeated He pulse irradiation. Blistering on W-V solid solute regions is mitigated than other two regions at 900 °C and microstructure evolution on W-V solid solute regions is delayed at 1800 °C. Furthermore, damage depth in W-V solid solute regions is smaller than that in W-enriched region and V-enriched region. In general, W-V solid solute region shows better surface damage resistance during the high heat flux He neutral beam irradiation.

The presented results indicate that W-V solid solute region behaves better after simultaneous He particle and high heat flux loading. W-V alloy developed for the advanced W-PFM is suggested to enlarge the fraction of W-V solid solute region and reduce the fraction of V-enriched region. The optimization will be done in our future work to obtain a better performance W-based material.

Acknowledgements

Special thanks to Dr. Kameel Arshad for the W-5V sample preparation.

Thanks for the support from National Nature Science Foundation of China under contract No. 11775015 and No. 51720105006.

Reference

[1] Lu G-H, Zhou H-B and Becquart C S 2014 A review of modelling and simulation of hydrogen behaviour in tungsten at different scales *Nucl. Fusion* **54** 86001

[2] Rieth M, Boutard J L, Dudarev S L, Ahlgren T, Antusch S, Baluc N, Barthe M F, Becquart C S, Ciupinski L, Correia J B, Domain C, Fikar J, Fortuna E, Fu C C, Gaganidze E, Galán T L, García-Rosales C, Gludovatz B, Greuner H, Heinola K, Holstein N, Juslin N, Koch F, Krauss W, Kurzydlowski K J, Linke J, Linsmeier C, Luzginova N, Maier H, Martínez M S, Missiaen J M, Muhammed M, Muñoz A, Muzyk M, Nordlund K, Nguyen-Manh D, Norajitra P, Opschoor J, Pintsuk G, Pippan R, Ritz G, Romaner L, Rupp D, Schäublin R, Schlosser J, Uytdenhouwen I, van der Laan J G, Veleva L, Ventelon L, Wahlberg S, Willaime F, Wurster S and Yar M A 2011 Review on the EFDA programme on tungsten materials technology and science *J. Nucl. Mater.* **417** 463–7

[3] Ueda Y, Schmid K, Balden M, Coenen J W, Loewenhoff T, Ito A, Hasegawa A, Hardie C, Porton M and Gilbert M 2017 Baseline high heat flux and plasma facing materials for fusion *Nucl. Fusion* **57** 92006

[4] Becquart C S and Domain C 2006 Migration energy of He in W revisited by Ab initio calculations *Phys. Rev. Lett.* **97** 1–4

[5] Roldán M, Fernández P, Rams J, Jiménez-Rey D, Ortiz C J and Vila R 2014 Effect of helium implantation on

mechanical properties of EUROFER97 evaluated by nanoindentation *J. Nucl. Mater.* **448** 301–9
[6] Cui S, Simmonds M, Qin W, Ren F, Tynan G R, Doerner R P and Chen R 2017 Thermal conductivity reduction of tungsten plasma facing material due to helium plasma irradiation in PISCES using the improved 3-omega method *J. Nucl. Mater.* **486** 267–73
[7] Ueda Y, Coenen J W, De Temmerman G, Doerner R P, Linke J, Philipps V and Tsitrone E 2014 Research status and issues of tungsten plasma facing materials for ITER and beyond *Fusion Eng. Des.* **89** 901–6
[8] Palacios T, Monge M A and Pastor J Y 2015 Tungsten-vanadium-yttria alloys for fusion power reactors (I): Microstructural characterization *Int. J. Refract. Met. Hard Mater.* **54** 433–8
[9] Arshad K, Zhao M-Y, Yuan Y, Zhang Y, Zhou Z-J and Lu G-H 2014 Thermal stability evaluation of microstructures and mechanical properties of tungsten vanadium alloys *Mod. Phys. Lett. B* **28** 1450207
[10] Arshad K, Wang J, Yuan Y, Zhang Y, Zhou Z-J and Lu G-H 2015 Development of tungsten-based materials by different sintering techniques *Int. J. Refract. Met. Hard Mater.* **50** 253–7
[11] Greuner H, Maier H, Balden M, Boeswirth B and Linsmeier C 2011 Investigation of W components exposed to high thermal and high H/He fluxes *J. Nucl. Mater.* **417** 495–8
[12] Yuan Y, Greuner H, Böswirth B, Linsmeier C, Luo G N, Fu B Q, Xu H Y, Shen Z J and Liu W 2013 Surface modification of molten W exposed to high heat flux helium neutral beams *J. Nucl. Mater.* **437** 297–302
[13] Du J, Yuan Y, Wirtz M, Linke J, Liu W and Greuner H 2015 FEM study of recrystallized tungsten under ELM-like heat loads *J. Nucl. Mater.* **463** 219–22
[14] Yuan Y, Greuner H, Böswirth B, Luo G N, Fu B Q, Xu H Y and Liu W 2013 Melt layer erosion of pure and lanthanum doped tungsten under VDE-like high heat flux loads *J. Nucl. Mater.* **438** 229–32
[15] Yuan Y, Xu B, Fu B Q, Greuner H, Böswirth B, Xu H Y, Li C, Jia Y Z, Qu S L, Luo G-N, Lu G H and Liu W 2014 Suppression of cavitation in melted tungsten by doping with lanthanum oxide *Nucl. Fusion* **54** 83026
[16] Ziegler J F, Ziegler M D and Biersack J P 2010 SRIM - The stopping and range of ions in matter (2010) *Nucl. Instruments Methods Phys. Res. Sect. B Beam Interact. with Mater. Atoms* **268** 1818–23
[17] Li C, Greuner H, Zhao S X, Böswirth B, Luo G N, Zhou X, Jia Y Z, Liu X and Liu W 2015 Micro-and nano-scale damage on the surface of W divertor component during exposure to high heat flux loads with He *J. Nucl. Mater.* **466** 357–61
[18] Li C, Greuner H, Yuan Y, Luo G N N, Böswirth B, Fu B Q Q, Xu H Y Y, Jia Y Z Z and Liu W 2014 Effects of temperature on surface modification of W exposed to He particles *J. Nucl. Mater.* **455** 201–6
[19] Tokunaga K, Tamura S, Yoshida N, Ezato K, Taniguchi M, Sato K, Suzuki S and Akiba M 2004 Synergistic effects of high heat loading and helium irradiation of tungsten *J. Nucl. Mater.* **329–333** 757–60
[20] Hammond K D 2017 Helium, hydrogen, and fuzz in plasma-facing materials *Mater. Res. Express* **4** 104002
[21] De Temmerman G, Hirai T and Pitts R A 2018 The influence of plasma-surface interaction on the performance of tungsten at the ITER divertor vertical targets *Plasma Phys. Control. Fusion* **60** 44018
[22] Li C, Greuner H, Yuan Y, Zhao S X, Luo G N, Böswirth B, Fu B Q B, Jia Y Z, Liu X and Liu W 2015 Surface modifications of W divertor components for EAST during exposure to high heat loads with He *J. Nucl. Mater.* **463** 223–7
[23] Hirohata Y, Yamada T, Yamauchi Y, Hino T, Nagasaka T and Muroga T 2006 Deuterium and helium retentions of V–4Cr–4Ti alloy used as first wall of breeding blanket in a fusion reactor *J. Nucl. Mater.* **348** 33–9
[24] Rainer Behrisch and Eckstein W 2007 *Sputtering by particle bombardment* vol 110
[25] Smirnov R D, Krasheninnikov S I and Guterl J 2015 Atomistic modeling of growth and coalescence of helium nano-bubbles in tungsten *J. Nucl. Mater.* **463** 359–62
[26] Krasheninnikov S I and Smirnov R D 2015 He cluster dynamics in fusion related plasma facing materials *Nucl. Fusion* **55** 73005
[27] Zhou H B, Wang J L, Jiang W, Lu G H, Aguiar J A and Liu F 2016 Electrophobic interaction induced impurity clustering in metals *Acta Mater.* **119** 1–8
[28] Becquart C S and Domain C 2012 Solute-point defect interactions in bcc systems: Focus on first principles

modelling in W and RPV steels *Curr. Opin. Solid State Mater. Sci.* **16** 115–25

[29] Li X C, Shu X, Tao P, Yu Y, Niu G J, Xu Y, Gao F and Luo G N 2014 Molecular dynamics simulation of helium cluster diffusion and bubble formation in bulk tungsten *J. Nucl. Mater.* **455** 544–8

[30] Wu X, Kong X-S, You Y-W, Liu C S, Fang Q F, Chen J-L, Luo G N and Wang Z 2013 Effects of alloying and transmutation impurities on stability and mobility of helium in tungsten under a fusion environment *Nucl. Fusion* **53** 73049

[31] Baldwin M J, Doerner R P, Wampler W R, Nishijima D, Lynch T and Miyamoto M 2011 Effect of He on D retention in W exposed to low-energy, high-fluence (D, He, Ar) mixture plasmas *Nucl. Fusion* **51** 103021

[32] Miyamoto M, Watanabe T, Nagashima H, Nishijima D, Doerner R P, Krasheninnikov S I, Sagara A and Yoshida N 2014 In situ transmission electron microscope observation of the formation of fuzzy structures on tungsten *Phys. Scr.* **T159** 14028

[33] Trinkaus H and Singh B N 2003 Helium accumulation in metals during irradiation – where do we stand? *J. Nucl. Mater.* **323** 229–42

[34] Kajita S, Yoshida N, Yoshihara R, Ohno N and Yamagiwa M 2011 TEM observation of the growth process of helium nanobubbles on tungsten: Nanostructure formation mechanism *J. Nucl. Mater.* **418** 152–8